Journal of Applied Electrochemistry **34**: 763–770, 2004.

The design and usage of a visual direct methanol fuel cell

JOAKIM NORDLUND[1]*, CYRIL PICARD[†], ERIK BIRGERSSON[2], MICHAEL VYNNYCKY[2] and GÖRAN LINDBERGH[1]

[1]*Department of Chemical Engineering and Technology, Applied Electrochemistry, KTH, SE-100 44 Stockholm, Sweden*

[2]*Faxén Laboratoriet, Department of Mechanics, KTH, SE-100 44 Stockholm, Sweden*

*(*author for correspondence, e-mail: joakim.nordlund@cellkraft.se)*

[†]*Present address: Laboratoire des écoulements géophysiques et industriels, ENSHMG, Grenoble, France*

Received 16 October 2003; accepted in revised form 1 March 2004

Key words: direct methanol fuel cell anode, gas evolution, porous medium, two-phase flow, visualization

Abstract

In order to better understand the influence of gas evolution on the performance of the direct methanol fuel cell (DMFC) anode, a visual DMFC, comprising of a transparent anode and a cathode endplate with an integrated heat exchanger, and a picture analysis methodology were developed. The result was an inexpensive, but very powerful, tool for analyzing the role of two-phase flow. An important finding is that gas bubbles do not appear uniformly throughout the fluid flow matrix, but rather only at a few active sites. Another important finding is that the gas saturation (volume fraction of gas/volume fraction of liquid) increases along the streamwise direction.

1. Introduction

Direct methanol fuel cells (DMFCs) constitute a promising alternative to batteries for a wide range of low power applications. Their major advantage over batteries is that they can be 'recharged' with a new fuel cartridge or just tanked up with fuel. In addition, the DMFC has the potential to store energy more compactly, decreasing weight and volume or increasing time of usage. Compared to the more mature hydrogen fed fuel cell, the DMFC comprises a simpler system with more compact and safe fuel storage of liquid methanol. The electrochemical reactions occurring in a DMFC are:

$$\text{Anode}: \quad CH_3OH + H_2O \rightarrow CO_2 + 6H^+ + 6e^- \tag{1}$$

$$\text{Cathode}: \quad 3/2O_2 + 6H^+ + 6e^- \rightarrow 3H_2O \tag{2}$$

$$\text{Sum}: \quad CH_3OH + 3/2O_2 \rightarrow CO_2 + 2H_2O \tag{3}$$

The carbon dioxide produced will, even at low current densities, exceed the saturation limit for carbon dioxide in water and evolve as a gas [1]. In a series of studies at University of Newcastle, the gas evolution on the anode side of a DMFC was investigated directly in the fuel cell using an end plate made of transparent acrylic plastic [2–5]. In those studies, different flow fields were tested [5] and the importance of a well-designed flow field [2, 4] was emphasized. It was also shown that the mass transfer of methanol to the anode active layer was reduced by the gas evolution [3]. Since mass transfer of methanol to the active layer has been shown to be very important for the DMFC performance [1, 6], it is important to study the influence of gas evolution on the performance to be able to reduce its adverse effects. There are, in principle, a number of possible measuring techniques that can be employed to study the influence of the gas evolution in the DMFC anode. Three of the most obvious are: probe insertion, the use of seeding particles and still photography.

Probing will always only give local information, so a number of probes have to be employed to give data along the anode. Probing is in principle an inexpensive and useful technique, but to insert a large amount of probes with the required precision into the anode end plate is costly. There is also the risk of influencing the behavior of the system, since the method is intrusive. Probing techniques that could be of interest in a study like this are: electrical probes, optical probes, capacitance probes and hot film anemometry.

By introducing seeding particles to the fluid stream, the flow can be characterized by laser doppler anemometry (LDA), phase doppler anemometry (PDA), particle tracking velocimetry (PTV) or particle image velocimetry (PIV). Applying these methods, the velocities of both

gas and liquid phases can be measured [7, 8]. Both LDV and PIV have earlier been applied successfully in an electrolysis system with current-induced gas evolution [9]. A drawback of these methods is that introducing seeding particles may well influence the performance of the anode, since there are pores of a wide range of sizes in the gas diffusion layer and the porous electrode itself where particles could block mass transfer.

The third option, to study pictures from a visual cell, is a simple and cost effective method. It does lack the possibility to analyze the phase velocities. The method gives the gas saturation at every point of the anode at any given time. Due to its simplicity, analyzing pictures from a visual cell is a good starting point for analyzing the influence of gas evolution on the performance of the anode. While the results obtained in the University of Newcastle studies are valuable [2–5], the methodology of analysis of the visual results can be improved. There, the pictures were converted to digital images and the subsequent analysis of the results was schematic, with no quantitative data being gathered from the visual data.

In this work we take the data analysis a step further, in that a methodology to acquire good visual data and to perform a high-quality and time effective analysis is presented. In particular, we demonstrate how a visual cell, in combination with digital video recordings and picture analysis, can be used to give valuable insight into two-phase flow in the anode of a DMFC.

2. Experimental

2.1. *The visual cell*

Just as in [2–5], our cell has a plexi-glass endplate on the anode side where the current is drawn out to the sides.

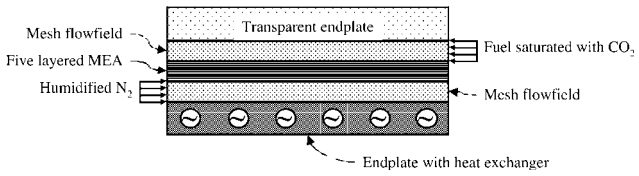

Fig. 1. The principle of the visual cell.

Figure 1 shows the principle of the visual cell. The potential drops due to the resistances in the spanwise direction of the stainless steel mesh and the current collector were computed and found to be less than 3 mV at 100 mA cm^{-2}. Thanks to the low spanwise potential drop in the mesh, the results from a visual cell can be applied to a DMFC with the same flow field length as the visual cell, regardless of the width of the flow field. To minimize the contact resistances between the current collectors and the stainless steel meshes, and between the mesh and the gas diffusion layer, the meshes and the current collectors were plated with a 10 μm thick layer of gold.

Since it is of interest to study the DMFC at a variety of temperatures, the cell was designed to give an even temperature distribution by introducing a circuit for cooling/heating directly behind the cathode, as shown in Figure 1. For the sake of temperature insulation and to provide an even clamping pressure on the flowfield mesh, the plexi-glass used in the cell is fairly thick (35 mm at the flowfield mesh). The flowfield mesh was a woven stainless steel mesh with the dimensions 1.50, 40, 130 mm in height, width and length, respectively, and had gaps with dimensions 1.35 × 1.35 mm. The porosity of the mesh was measured to be 0.87. The cell, mesh, MEA, gaskets and anode current collector are shown in Figure 2.

Since the buoyancy of the carbon dioxide bubbles is expected to have an impact on the performance of the DMFC, the visual cell was mounted on a rack, to allow for measurements at different cell tilting angles. In this study, however, all experiments were carried out in horizontal mode as the data were to be compared to model predictions by a two-dimensional two-phase model of a cell running in horizontal mode (Birgersson et al., submitted for publication).

2.2. *The system and experimental conditions*

In addition to the visual cell, the system comprises a peristaltic pump (Watson Marlow), a humidifier (Fuel Cell Technologies, Inc.), a pre-heater, a fuel reservoir, a circuit for cooling/heating water, a phase separator, pressure probes and means to measure gas- and liquid flows.

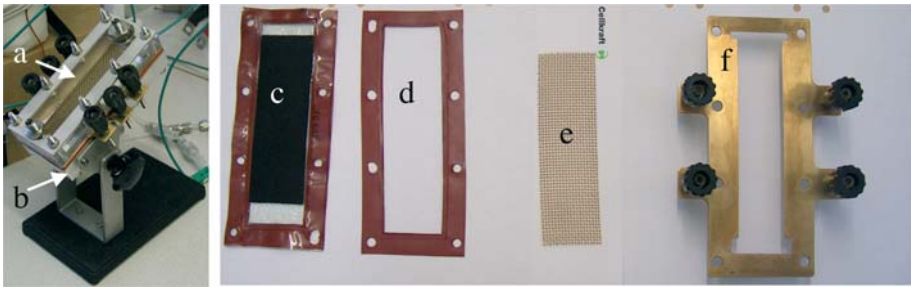

Fig. 2. The visual cell: (a) transparent acrylic plastic end plate; (b) aluminum endplate with integrated heat exchanger; (c) five-layer MEA with sealing gasket; (d) sealing gasket; (e) gold plated mesh; (f) gold plated anode current collector.

All measurements were performed with the visual cell, shown in Figure 2, in horizontal mode. The membrane-electrode-assembly (MEA), manufactured by BCS Fuel Cells Inc., has a noble metal loading of 1.6 mg cm^{-2} PtRu on the anode (1:1, 60% on C) and 1.6 mg cm^{-2} Pt on the cathode (60% on C). The thickness of the anode was 14 μm, measured with SEM, and the membrane was Nafion 117. The MEA has five layers, with the carbon cloth gas diffusion layer attached directly to the electrodes. The MEA with a 40×120 mm^2 active layer was produced from the same batch as the 1 cm^2 MEA characterized in a separate study (Nordlund and Lindbergh, submitted for publication).

The cathode reaction in all experiments was hydrogen evolution, as given in Equation 4:

$$\text{Cathode}: \quad 6H^+ + 6e^- \rightarrow 3H_2 \tag{4}$$

Hydrogen evolution was chosen in order to minimize the losses on the cathode and to have a relatively stable cathode potential due to the fast hydrogen evolution kinetics.

All measurements were run in galvanostatic mode with a current source; the potential was recorded on a x–t recorder and digitized with a picture analysis scheme similar to the one described in the methodology section below. Only cell voltage was measured; thus, all the given potentials are cell voltages. The noise in the experimental data is within ± 5 mV. All experimental data are taken under steady-state conditions. At low current densities, steady state could be reached after about 100 s, whereas up to 1000 s could be necessary for higher current densities. Humidified N_2 (5.0) was fed to the cathode side, with a saturation temperature 15° above the temperature of the cell at a low flow rate. The methanol/water fuel mixture was preheated to the temperature of the cell and saturated with CO_2. A 1 M methanol solution was used in all experiments (pro analysi, Merck and MilliQ water).

A DV-camera with 25 Hz time resolution and 576×720 pixel resolution (SONY TRV900) was mounted on a tripod. A lamp was aimed away from the cell and its light made to reflect off a white fabric approximately 40 cm from the cell to obtain appropriate lighting conditions for the recordings. The quality of the movies shot hinged on finding lighting conditions and camera viewing angle to obtain the best contrast between the gaseous phase and the liquid phase. MATLAB 6.5 was used for the picture analysis.

3. Methodology – movie analysis

The methodology to extract the visual information from the digital video recordings involves a three-step procedure: pre-processing, frame analysis and post-analysis. Each picture frame is stored in MATLAB as a $576 \times 720 \times 3$ matrix where the third dimension contains information about the intensity of the colors RGB (red, green and blue) from 0 to 255. We define the brightness, v, as

$$v = \frac{1}{3}(R + G + B) \tag{5}$$

where R, G and B are the respective intensity of the colors.

3.1. *Pre-processing*

During the experiments, the gas will appear brighter than the transparent liquid over the dark gas diffusion layer when the lighting conditions and viewing angle are optimized, as is illustrated in Figure 3, depicting a typical frame from the DV-camera during experiments. As can be discerned from Figure 3, it is difficult to differentiate the gold plated mesh wires from the mesh gaps filled with gas. The aim of the pre-processing step is to determine the position of the mesh and to store its position, pixel by pixel, in a matrix. This proved to be the most complex step of the analysis and was carried out as follows: a liquid solution was pumped through the mesh flow field on the anode to remove all the gas bubbles, which might be trapped in the mesh; then, a picture was then taken, showing the mesh wires on top of the dark gas diffusion layer. Even though the gold plated wires appear bright in contrast to the dark gas diffusion layer, the wire intensity varies considerably, since the wires are round and woven; thus, a simple brightness threshold was not sufficiently accurate to pinpoint the pixels corresponding to the mesh. In Figure 4a, a pixel-by-pixel close-up of the mesh with no gas is shown. Figure 4b illustrates the result of a simple black and white threshold on the previous picture. The simple threshold does not result in a perfect digital representation of the mesh. Therefore, a wire recognition program was implemented in MAT-

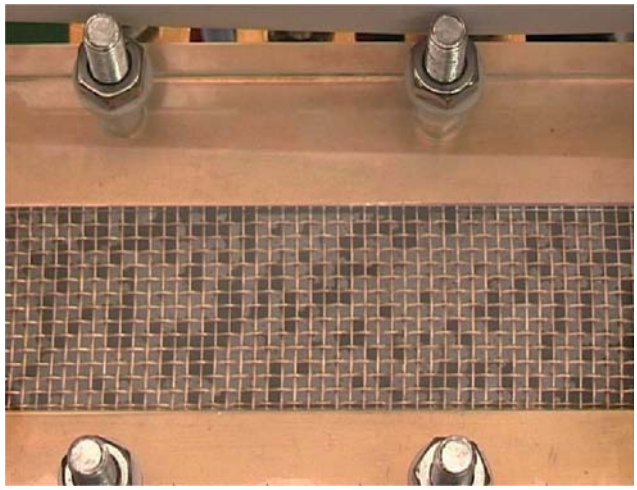

Fig. 3. Typical picture from DV-camera.

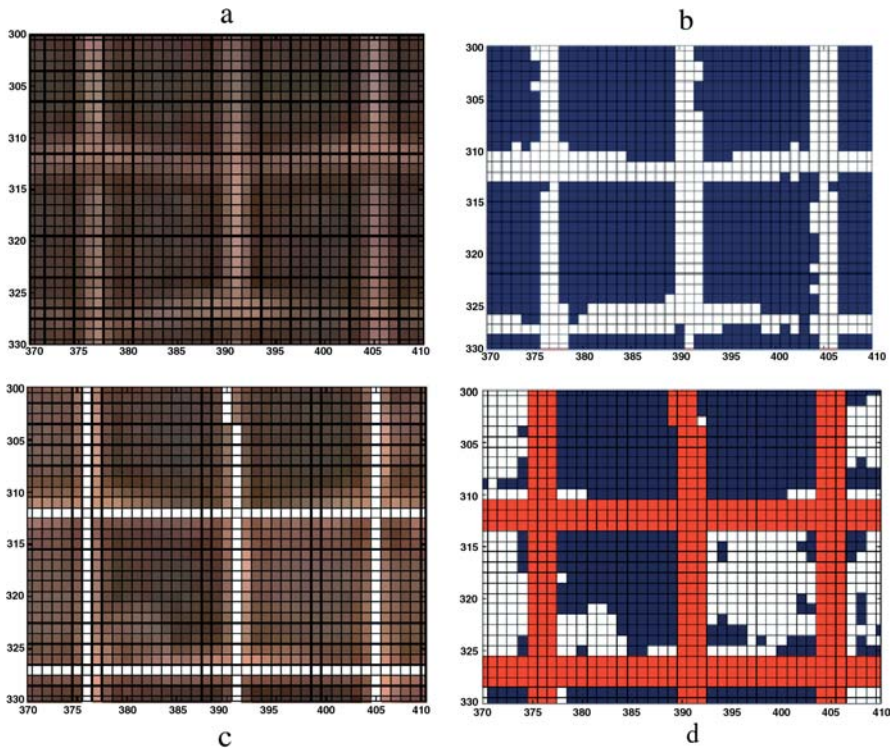

Fig. 4. Details of the picture analysis: (a) a close-up with no gas; (b) a simple threshold on the previous picture, where the mesh position is given by the white pixels and the mesh gaps by the black pixels; (c) a picture with gas with the mesh centre position marked in white; (d) the analysis of the previous picture, where the white pixels are recognized as gas, the black pixels are recognized as liquid and the grey pixels denote the mesh wire.

LAB 6.5 to identify the centers of the mesh wires. The identified grid center is shown in Figure 4c. The grid removed from the processed pictures is three pixels wide with the center taken as the center position of the mesh, as identified by the MATLAB program (see Figure 4d).

3.2. *Frame analysis*

When studying a snapshot of the movie, as in Figure 3, it is obvious that partially filled mesh gaps occur significantly less frequently than mesh gaps that are either completely filled with only gas or liquid. This observation allows a simplification of the frame analysis, since each gap thus can be considered to be filled with either gas or liquid. We define a reduced binary $M \times N$ matrix, where M and N are the number of mesh gaps in the picture in the streamwise and spanwise directions, respectively. As shown in Figure 4d, the mesh position is known, and is removed from the full data matrix before the analysis. The brightness of every pixel in the mesh gap, (see Figure 4c), is compared to a threshold value above and below which the pixel is considered white and below, respectively; the resulting matrix is shown in Figure 4d. A simple majority of either white or black pixels in a mesh gap could determine whether or not the mesh gap should be considered as containing gas or liquid, although it was found that a higher precision was achieved, if the simple majority criterion was abandoned. Instead, a 60% criterion was applied, where the mesh gap was considered to 'change' color only when more than 60% of the pixels in the gap had done so.

3.3. *Post-analysis*

To ensure that the software captures and differentiates the liquid- from the gas-filled gaps, a verification image, produced by the software for every 10th frame, was visually examined. Figure 5 depicts such a verification image, where the recognition results are given as white (gas) or black (liquid) dots in the actual picture. In the case of a mismatch, the brightness threshold was re-evaluated; this, however, rarely occurred during the analysis of one film, but if the camera position and

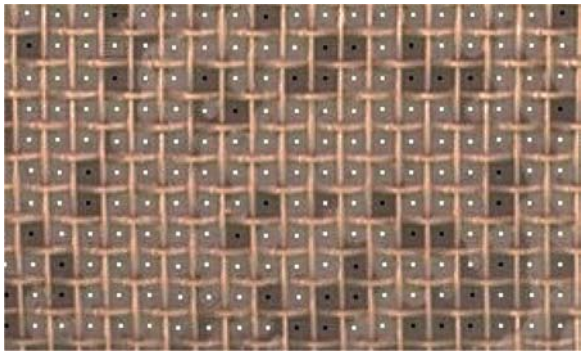

Fig. 5. The verification image for the automated gas recognition.

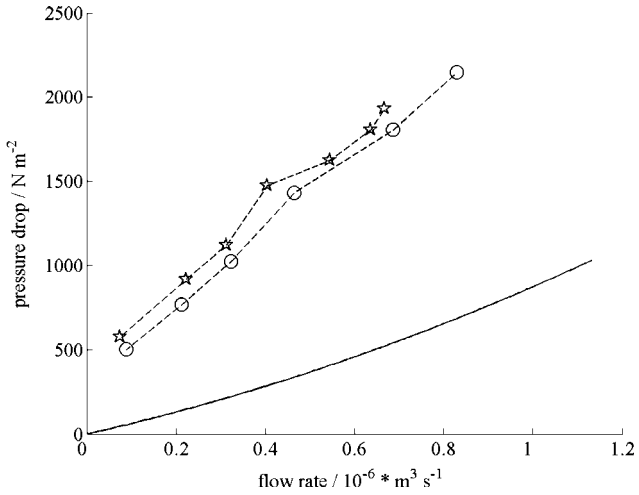

Fig. 6. Pressure drop as a function of the inlet flow rate: (—) no current; 45 °C; (○) 68 mA cm^{-2}; 45 °C; (☆) 79 mA cm^{-2}; 45 °C.

resulting lighting conditions were changed between measurements, then the threshold value had to be changed.

4. Results

In Figure 6, the pressure drop over the anode is given as a function of the inlet fuel flow rate. When a current is applied gas bubbles start to appear and affect the flow pattern in the flow field. Increasing the current density increases the pressure drop.

Figure 7 depicts the measured mass balance of CO_2 over the anode as a function of the current density. We define Δ as the amount of CO_2 exiting the anode as a gas, measured with a gas flow meter outside of the cell, divided by the amount of CO_2 produced, assuming 100% current efficiency, i.e.

$$\Delta \equiv \frac{\dot{m}_{CO_2}^{out}}{1 * M_{CO_2}/6F} \tag{6}$$

where $\dot{m}_{CO_2}^{out}$ is the mass flux of CO_2 out of the anode, I is the current, M_{CO_2} is the molar mass of CO_2 and F is Faraday's constant. For current densities lower than 25 mA cm^{-2}, Δ is less than 0.5, indicating that less than 50% of the CO_2 produced exits the anode as a gas, even though the liquid fuel at the inlet is CO_2-saturated. Increasing the liquid flow by approximately a factor of four, from 1.3×10^{-7} to 4.5×10^{-7} m^3 s^{-1}, only resulted in a small change in Δ.

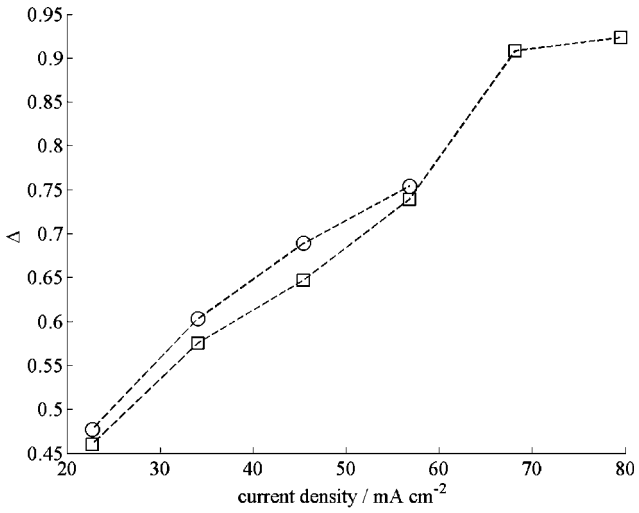

Fig. 7. Value of Δ as a function of current density. Temperature is 45 °C and flow rates are (○) 1.3×10^{-7} m^3 s^{-1} and (□) 4.5×10^{-7}m^3 s^{-1}.

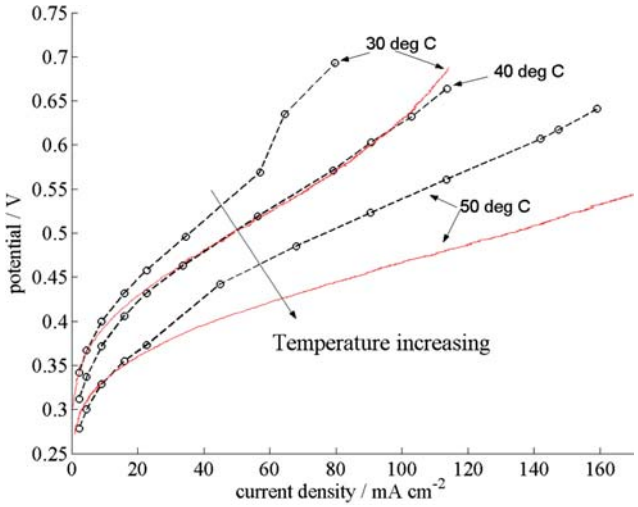

Fig. 8. Polarization curve for $T = 30$, 40 and 50 °C at a fuel flow rate of 4.4×10^{-7} m^3 s^{-1} (-○-). The solid lines (—) denote experimental data from a 1 cm^2 DMFC with a MEA of identical composition at high stoichiometric excess at 30 and 50 °C (Nordlund and Lindbergh, Submitted for publication).

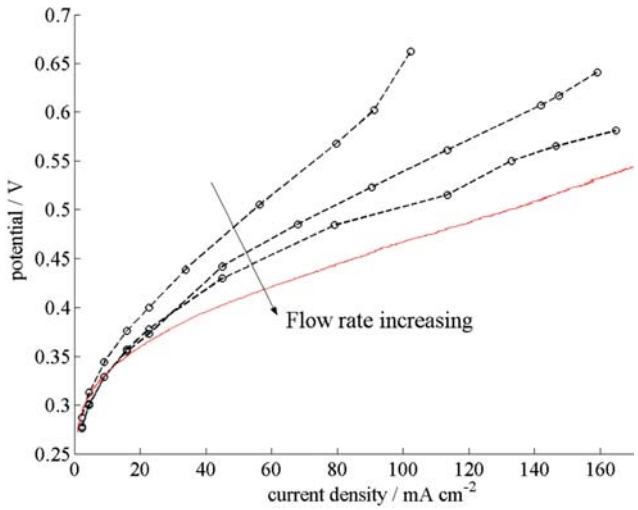

Fig. 9. Polarization curves for different fuel flow rates (0.06×10^{-6}, 0.44×10^{-6} and 1.00×10^{-6} m^3 s^{-1}) at 50 °C. The solid line (—) denotes experimental data from a 1 cm^2 DMFC with a MEA of identical composition at high stoichiometric flow at 50 °C (Nordlund and Lindbergh, Submitted for publication).

Figures 8 and 9 show polarization curves as a function of current density and flow rate. To Figure 8 we have added the experimental results from another study where a 1 cm^2 MEA with the identical composition was studied and the kinetic rate constants of the MEA were extracted (Nordlund and Lindbergh, submitted for publication). In that study a DHE reference electrode was used. Figure 8 shows how the performance increases with increasing temperature. In Figure 9 the increase in performance when flow rate is increased is shown. The performance approaches that of the high stoichiometry 1 cm^2 experimental data at high flow rates.

Figure 10 shows the grid displayed through a magnifying glass. The static bubbles in Figure 10 appear brighter due to methanol/water vapor condensation at the transparent endplate. The fuel flow rate in this experiment is low (8.5×10^{-8} m^3 s^{-1}), as is the current density (10 mA cm^{-2}). An important observation is that the gas does not evolve homogeneously across the surface; gas nucleation is mostly confined to a few active sites. All the gas appearing after $t = 0$ in Figure 10a–d originates from the site marked with a white arrow. In fact, closer examination of the movies reveals that the vast majority of such active sites are located in corners where the wires of the mesh intersect.

On a local scale, the gas flow is intermittent, with gas residing in a mesh gap for hundreds of seconds in the case of the least active mesh gaps. For the most active mesh gaps, the entrapment time can be as low as a few seconds. On a global scale, the flow of gas is much more even. From the experiments it is observed that the time for a change of state, from gas-filled liquid-filled state, differs depending on the initial state. In an attempt to characterize this behavior, we have measured for each grid point throughout the flow field the time between when bubbles emerge and disappear and the time between the disappearance and reappearance of a bubble in the mesh gap. Figure 11 shows that the time between the disappearance of one bubble and the appearance of a new one at the same location remains fairly constant with varied fuel flow rates, and is low compared to the time between appearance and disappearance, which is more strongly influenced by the fuel flow rate. To simplify the illustration, it was chosen to present the time for which 90% of the mesh gaps had changed their state, denoted t_{90}.

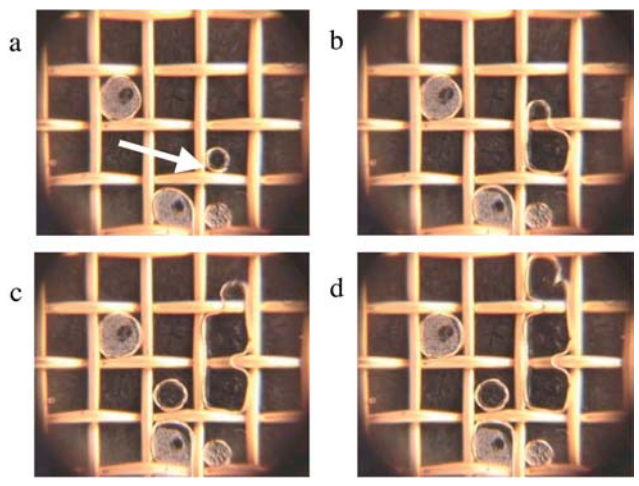

Fig. 10. Local effect of bubble nucleation: gas-phase expansion from an active mesh site at (a) $t = 0$, (b) $t = 3$ s, (c) $t = 9$ s and (d) $t = 11$ s. The white arrow marks the active gas-producing mesh site. The current density is 10 mA cm^{-2} and the temperature is 45 °C. The fuel flows from the right to the left with a flow rate of 8.5×10^{-8} m^3 s^{-1}.

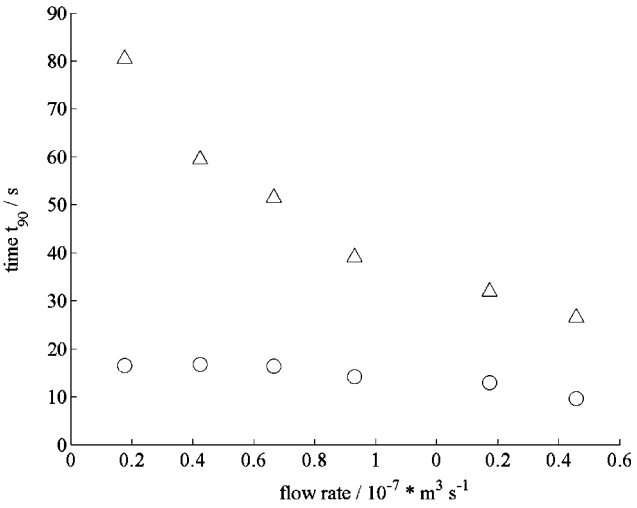

Fig. 11. Illustration for the change of state at 45 °C and 68 mA cm^{-2} as a function of fuel flow rate: (○) necessary time to observe disappearance and reappearance of a bubble in 90% of the mesh gaps, (Δ) necessary time to observe appearance and disappearance of a bubble in 90% of the mesh gaps.

Figure 12a–c illustrates the local differences in frequency for changing state from liquid to gas for three different fuel flow rates. The figure is three-dimensional in the sense that it shows the frequency of changing state for each individual mesh gap in the analyzed digital movie. The dark pixels corresponds to mesh gaps where there was very seldom state-change, or not at all, during the measurement, whereas the brighter pixels corresponds to mesh gaps that change state between liquid and gas much more frequently.

Figure 13 show the spanwise average of the time-averaged gas saturation for each individual mesh gap as a function of the streamwise position; the time interval used for averaging was approximately 240–300 s. Even though the data appears to be somewhat dispersed, the trend that the time averaged gas saturation increases along the streamwise axis of the fuel cell is clear. Figure 13 also shows that a higher fuel flow rate reduces the gas saturation.

5. Discussion

Figure 6 shows a considerable increase in pressure drop when a current is drawn. This increase can be attributed to the carbon dioxide gas production, which takes place as a current is passed through the cell. The employed mesh flow field traps the bubbles in the mesh gaps, as seen

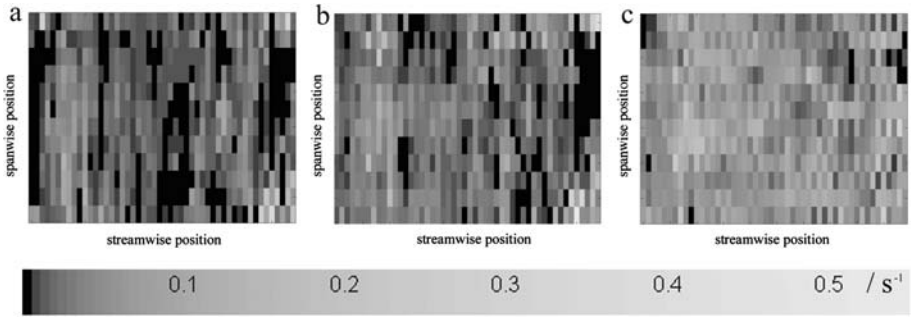

Fig. 12. Frequency for changing state from liquid to gas for recorded mesh gaps. Each pixel corresponds to a physical gap in the mesh. The temperature is 45 °C and the current density is 68 mA cm^{-2}. The fuel flows from left to right and the rate is: (a) 8.5×10^{-8} m^3 s^{-1}, (b) 3.2×10^{-7} m^3 s^{-1} and (c) 8.0×10^{-7} m^3 s^{-1}.

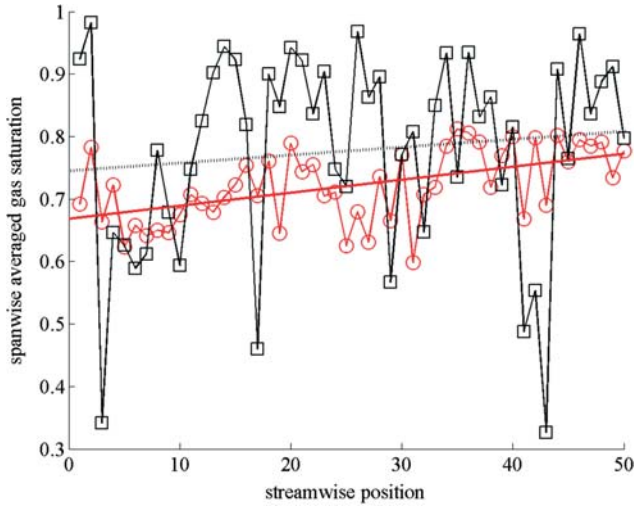

Fig. 13. Streamwise gas saturation at 45 °C and 68 mA cm^{-2}. Fuel flow rates are (□) 8.5×10^{-8} m^3 s^{-1} and (○) 8.0×10^{-7} m^3 s^{-1}. The dotted trend line corresponds to the lower fuel flow rate. Trend lines were fitted with MATLAB.

in Figure 12, resulting in a reduced cross-section for liquid-phase flow. Taking an average gas saturation of about 0.7–0.8 from Figure 13 and assuming that the gas blocks the way for the liquid, then the local liquid flow rate in the free passage in the mesh would increase considerably, due to lessened free passage and increased tortuosity. It is reasonable that this increase in local liquid flow rate leads to a substantial increase in pressure drop.

At low current densities, less than 50% of the produced carbon dioxide is accounted for in the anode exhaust according to Figure 7. Since the fuel is saturated with CO_2 before entering the cell, there are two possible reasons for this observation: mass transport through the membrane to the cathode side or a low current efficiency for carbon dioxide production. The latter is less likely since the fraction accounted for in the exhaust approaches 100% at higher current densities. It has been show earlier that the concentration of CO_2 in the anode active layer may be well over the solubility limit, as the pores are too small to allow CO_2 gas nucleation [6, 10]. This supersaturated carbon dioxide can travel one of two ways: through the membrane over to the cathode side, where the partial pressure of carbon dioxide is virtually zero, or through the gas diffusion layer, along the streamwise direction of the mesh and through the anode outlet. The major contributions to the mass transfer resistance on the anode side are due to diffusion through the gas diffusion layer to the mesh where CO_2-saturated fuel flows and transport through the mesh to the outlet. The latter should not be underestimated, as the fuel is saturated and the velocity of the gas, hindered by the mesh, is very low.

Qualitatively, the results shown in Figure 8 agree well with those in a separate work, where the kinetics of the electrode were deduced in a 1 cm^2 DMFC (Nordlund and Lindbergh, submitted for publication). The agreement is best at low current densities (less than 20 mA cm^{-2}), where depletion of methanol along the streamwise position is negligible because of high stoichiometry. The observation in Figure 9 that the performance at higher flow rates approaches the 1 cm^2 cell data supports that conclusion.

None of the results displayed in Figures 6–9 are unique for experiments with a visual cell. Nevertheless, by using a visual DMFC, the results may be interpreted in the light of the specific knowledge obtained, thanks to the data from the visual investigation. For instance, the increase in pressure drop seen in Figure 6 can be directly linked to the observed stationary gas bubbles reducing the free passage for the flow of liquid fuel.

A very interesting observation in this work is that the gas (produced in the active layer and transported through the gas diffusion layer) appears in the flow field far from homogeneously. Figure 10 shows an active mesh cell and the surrounding passive cells. The movement of the gas from one mesh cell to the downstream adjacent cell is also shown. The fact that the vast majority of such active sites are located in mesh corners, where wires intersect, is not very surprising, considering that the gas diffusion layer at those points is more compressed. This compression will result in reduced contact resistance between the mesh and the gas diffusion layer; in addition the mass transfer of methanol and carbon dioxide is enhanced.

As expected, there are fewer inactive mesh gaps and generally higher frequencies for state change from liquid

to gas when the fuel flow rate is higher, as seen in Figure 12. Keeping the local differences shown in Figure 12 in mind, it is easier to understand the apparent randomness in Figure 13. Figure 13 shows that the gas saturation increases in the streamwise direction of the fuel cell and that the gas saturation decreases for higher flow rates. This result makes sense: the gas saturation should be higher along the streamwise direction since gas is produced along the axis. In addition, the gas saturation should be lower when liquid flow rate is higher, since the liquid is then more easily able to push the gas forward, and thereby preventing entrapment in the mesh.

To improve the performance of the DMFC, knowledge of the nature of the limiting factors within the DMFC anode is important. Here modeling of the anode will play an important part. The methodology presented can play a vital role in the acquisition of the visual data needed to verify the two-phase flow models. A good model should not only be able predict polarization curves well; its two-phase predictions should also match experimental reality.

Parameters that it will be of interest to vary in future experiments and models are the flow matrix, surface tension and the gas-backing material. In addition, the influence of oscillating fuel pressure with different frequencies and amplitudes, as well as operation in vertical mode, should be investigated. The methodology can also be used to provide knowledge about the CO_2 concentration gradients in the system. For instance, by using a high speed DV-camera more rapid phenomena, such as the implosion of bubbles that is observed when the current is interrupted, can be studied in more detail to give valuable insight into the actual CO_2 concentration gradients.

6. Conclusions

A visual DMFC system and a methodology to extract useful data from DV-camera recordings were developed. From the experiments and analysis of the employed method the following can be concluded:

At low current densities, a large fraction of the carbon dioxide produced is not transported out with the liquid flow, but rather transported through the membrane to the cathode side. The gas bubbles do not move continuously: they form, grow to the neighboring sites and are finally swept away with the liquid flow. The fact that the bubbles are, in a sense, trapped in the mesh gaps leads to a sharp increase in pressure drop when a current is drawn, as compared to an all-liquid system.

Gas bubbles tend to form at several active mesh gaps, which are more or less randomly located in the mesh. These active mesh gaps have a large influence on the result when studying gas saturation or frequency of changing state between liquid and gas; moreover, the results appear to be random. A consequence is that a visual cell with a mesh flow field should have more mesh gaps in the spanwise direction than the cell used in this work to decrease the uncertainty in the data.

Despite the randomness of the local data, a clear trend can be seen: the gas saturation increases along the streamwise direction in the fuel cell. This is an important result that can be used to verify two-phase flow models of the anode.

The combination of a visual DMFC and a DV-camera is a very simple, affordable, yet powerful, tool and methodology to study and improve the direct methanol fuel cell.

Acknowledgements

Financial support from the Swedish Foundation for Strategic Environmental Research, MISTRA, and from the Swedish National Energy Administration is gratefully acknowledged. The work was done within the framework of the Jungner Center. J. Nordlund gratefully acknowledges the scholarship from the Ernst Johnson foundation.

References

1. E. Birgersson, J. Nordlund, H. Ekström, M. Vynnycky and G. Lindbergh, *J. Electrochem. Soc.* **150** (2003) A1368.
2. P. Argyropoulos, K. Scott and W.M. Taama, *J. Appl. Electrochem.* **29** (1999) 661.
3. K. Sundmacher and K. Scott, *Chem. Eng. Sci.* **54** (1999) 2927.
4. P. Argyropoulos, K. Scott and W.M. Taama, *Electrochim. Acta* **44** (1999) 3575.
5. K. Scott, P. Argyropoulos, P. Yiannopoulos and W.M. Taama, *J. Appl. Electrochem.* **31** (2001) 823.
6. J. Nordlund and G. Lindbergh, *J. Electrochem. Soc.* **149** (2002) A1107.
7. C. Crow, M. Sommerfeld and Y. Tsuji, 'Multiphase Flow with Droplets and Particles' (CRC Press, Boca Raton, 1998).
8. F.T.M. Nieuwstadt (Ed), 'Flow Visualization and Image Analysis' (Delft, The Netherlands, 1993).
9. P. Boissonneau and P. Byrne, *J. Appl. Electrochem.* **30** (2000) 767.
10. J. Nordlund, A. Roessler and G. Lindbergh, *J. Appl. Electrochem.* **32** (2002) 259.